International Journal of Thermal Sciences, Volume 84, October 2014, Pages 75–85

Application of a high density ratio lattice-Boltzmann model for the droplet impingement on flat and spherical surfaces

Duo Zhang[1,2], K. Papadikis[1*], Sai Gu[1]

[1] *Xi'an Jiaotong-Liverpool University, No. 111 Ren'ai Road, Suzhou Dushu Lake Higher Education Town, Suzhou, China 215123.*

[2] *The University of Liverpool, Brownlow Hill, Liverpool, L69 7ZX, United Kingdom.*

Tel: 0086-512-88161752

Email: Konstantinos.Papadikis@xjtlu.edu.cn

∗Corresponding author

Abstract

In the current study, a 3-dimensional lattice Boltzmann model which can tolerate high density ratios is employed to simulate the impingement of a liquid droplet onto a flat and a spherical target. The four phases of droplet impact on a flat surface, namely, the kinematic, spreading, relaxation and equilibrium phase, have been obtained for a range of Weber and Reynolds numbers. The predicted maximum spread factor is in good agreement with experimental data published in the literature. For the impact of the liquid droplet onto a spherical target, the temporal variation of the film thickness on the target surface is investigated. The three different temporal phases of the film dynamics, namely, the initial drop deformation phase, the inertia dominated phase and the viscosity dominated phase are reproduced and studied. The effect of the droplet Reynolds number and the target-to-drop size ratio on the film flow dynamics is investigated.

Published by Elsevier. This is the Author Accepted Manuscript issued with:
Creative Commons Attribution Non-Commercial No Derivatives License (CC:BY:NC:ND 3.0).
The final published version (version of record) is available online at 10.1016/j.ijthermalsci.2014.05.002. Please refer to any applicable publisher terms of use.

Keywords: Multiphase flow, Lattice Boltzmann, high-density-ratio, droplet impact, spread factor, film thickness

1 Introduction

The droplet impingement on a solid surface is a common phenomenon, such as rain drops falling on the ground, ink-jet printing, spray cooling of hot surfaces, spray painting and coating, plasma spraying, fuel spray in combustion chamber, catalytic processing in fixed bed reactors and more recently in microfabrication and microchannels [1]. Therefore, research on droplets impacting on a solid surface attracts great interest from researchers. Rein [2] presented a comprehensive review on this phenomenon. Systematic studies have been carried out by Rioboo et al [3], where six possible outcomes of drop impact on a dry wall were revealed, namely deposition, prompt splash, corona splash, receding break-up, partial rebound and complete rebound. The influence of the droplet size, impact velocity, droplet viscosity, interfacial surface tension, surface roughness amplitude and surface wettability characteristics on the impingement process have been investigated. To systematically study the dynamics of a spreading droplet, three major non-dimensional parameters are usually employed, specifically the Weber number (We), Reynolds number (Re) and the Ohnesorge number (Oh) which is also directly related to We and Re. They are defined as

$$We = \frac{\rho_L D_0 U_0^2}{\sigma}, \tag{1}$$

$$Re = \frac{\rho_L D_0 U_0}{\mu_L}, \tag{2}$$

$$Oh = \frac{\mu_L}{\sqrt{D_0 \sigma \rho_L}} = \frac{\sqrt{We}}{Re}, \tag{3}$$

where U_0 is the drop impaction speed, D_0 is the diameter of the spherical drop prior to impact, μ_L is the liquid viscosity, σ is surface tension of the interface between liquid and gas, and the ρ_L is liquid density. The spread factor, which is an effect of the impact process, is defined as the ratio of the total diameter of the spreading droplet (not the

lamella diameter) and the initial droplet diameter:

$$D^{\star} = \frac{D}{D_0}. \tag{4}$$

Experimental and analytical investigations have been performed to study the time evolution of the spread factor and to determine the correlation between the maximum spreading factor and the Weber, Reynolds and Ohnesorge numbers [4–9]. The maximum spreading factor is defined as $D^{\star}_{max} = D_{max}/D_0$, where D_{max} is the maximum diameter of the contact area of the drop on the substrate. Asai et al. [4] examined the spreading of a micron size droplet from an inkjet printhead impacting on moving paper and obtained a simple correlation formula to predict the maximum spreading ratio. Scheller and Bousfield [5] showed that the contact angle effect on the spreading film diameter is negligible for droplet Re >10, and that the maximum spread factor follows the correlation given by $D_{max} = 0.61(Re^2Oh)^{0.166}$. Roisman et al. [9] modeled the drop impaction process to predict the evolution of the drop diameter. The model accounts for the capillary force, viscosity and inertial effects, as well as the dynamic contact angle. Micron drop impaction on smooth solid substrates was investigated by Dong [10] over a wide range of impaction speeds, surface contact angles and drop diameters. The experimental results were compared with several existing equations for predicting maximum spreading. The prediction equation of Roisman et al. [9] agrees well with the experimental results for both low and high We impactions. The empirical equation of Scheller and Bousfield [5] also gave a good fit even though the effect of the equilibrium contact angle was neglected. Previously published work [11–13] has shown that the impaction of droplets onto curved surfaces (e. g spheres), differs significantly from the impact of droplets on large substrates. The studies for the droplet impact onto curved surfaces will have enormous utility in several industrial applications, such as tablet coating, encapsulation processes and catalytic processing in fixed beds. Hung and Yao [11] have carried out experiments on the impaction of water droplets with diameters of 110, 350 and 680 μm on cylindrical

wires. The effects of droplet velocity and wire sizes were studied parametrically to reveal the impaction characteristics. Bakshi et al. [13] have reported experimental data and theoretical investigations on the impact of a droplet onto a spherical target over a range of Reynolds numbers and target-to-drop size ratios. Three distinct temporal phases of the film dynamics were found, namely the initial drop deformation phase, the inertia dominated phase, and the viscosity dominated phase. The influence of the droplet Reynolds number and the target-to-drop size ratio on the dynamics of the film flow on the surface of the target were conducted.

Recently, numerical investigations have drawn increasing attention in simulating the impingement process, because experiments alone are not adequate enough to define the governing physics [14]. Trapaga and Szekely [15] used a commercial code (FLOW-3D) that incorporates the "volume of fluid"(VOF) method to study the impact of molten particles in the thermal spray process. Bussmann et al. [16] studied the dynamics of droplet impact on flat and inclined surfaces with a 3D VOF method. As a modern method, lattice Boltzmann method (LBM) has attracted considerable attention in simulating the droplet impingement on solid surfaces. Gupta and Kumar [17, 18] studied the droplet impingement on a flat solid surface at low density ratios. Yan and Zu [19] reported a new numerical scheme for the lattice Boltzmann method, which combines the existing model of Inamuro et al. [20] and Briant et al. [21] for calculating the liquid droplet behavior on partial wetted surfaces, typical for large density ratios gas-liquid systems. However, Inamuro et al.'s model [20] involves the solution of Poisson equation, which decreases the simplicity of the usual LBM. Moreover, Fakhar and Rahimian [22] found that the free-energy-based model [23] is not capable of dealing with two-phase flows with different densities and is mostly suitable for binary fluids for which the Boussinesq approximation holds. Until now, most of the studies focus on flat and inclined solid surfaces. Few studies focus on the simulation of a droplet impact on a curved surfaces. Shen et al. [24] adopted the two-dimensional lattice Boltzmann pseudo-potential method to simulate the droplets impacting on curved solid surfaces. However, the gas-liquid density ratio is limited to

unity.

In the current study, we apply a 3-dimensional lattice Boltzmann model based on the original Shan-Chen model [25] and the improvements in the single-component multiphase flow model reported by Yuan and Schaefer [26] to study the impaction of a liquid droplet on a dry flat surface and a curved surface for a liquid-gas system with large density ratio. The influence of Reynolds number, Weber number, Ohnesorge number and the target-to-drop size ratio on the impingement process is reported. The results are compared with experimental data reported in the literature.

2 Numerical Method

In recent years, LBM has become a promising numerical technique for the simulation of multiphase flows due to its local nature of interactions. Unlike traditional CFD, it does not need to track or construct the vapor-liquid interface. Several models have been developed for multiphase and multi-component flows during the last twenty years, such as Rothman and Keller's color method [27], Shan et al's potential method [25], Swift et al.'s free energy method [23] and He et al.'s phase field method [28]. However, all of the above LBM models are limited to small density ratios, usually less than ten, due to numerical instabilities. To overcome this difficulty, Reis and Phillips [29] changed the forcing scheme of the perturbation operator based on the color method to induce the appropriate surface tension term in the macroscopic equations. Leclaire et al. [30] adapted the recoloring operator for the Reis and Phillips model in the case of variable density ratios and this model could be used to simulate flows with large density ratios in some test cases. Leclaire et al. [31] modified the original equilibrium distribution functions to capture the momentum discontinuity in the two-layered Couette flow with large density ratio. Inamuro et al. [20] proposed a model based on the free energy method for multiphase flows with large density ratio. However, in this model, the pressure correction is applied to enforce the continuity condition after every collision-streaming step, which is similar

to the VOF method and the level set method. The projection step would reduce the efficiency of the method greatly [32]. Lee and Lin [33] achieved a high density ratio by improving Swift's free-energy model [23] and the model of He et al. [28], respectively. Zheng et al. [34] proposed a method for simulating multiphase flows with high density ratio based on the free-energy approach. Recently, Fakhar and Rahimian [22] found that this model is not capable of dealing with two-phase flows with different densities and is mostly suitable for binary fluids in which the Boussinesq approximation holds. Recently, Yuan and Schaefer [26] expressed that the equation of state (EOS) plays an important role in achieving high-density ratios. Thus, the incorporation of the Peng-Robinson equation of state into the Shan-Chen [25] multiphase lattice Boltzmann model is adopted in the present study.

2.1 Pseudo-potential model

The particle distribution function is governed by the discretized Boltzmann equation with single relaxation time for the collision term [35]:

$$f_\alpha(\boldsymbol{x}+\boldsymbol{e}_\alpha\delta t, t+\delta t) = f_\alpha(\boldsymbol{x},t) - \frac{1}{\tau}[f_\alpha(\boldsymbol{x},t) - f_\alpha^{eq}(\boldsymbol{x},t)], \tag{5}$$

where f_α is the particle distribution function along the αth direction, f_α^{eq} is equilibrium distribution function, δt is the time step, $\boldsymbol{e}_\alpha$ is the particle velocity in the αth direction, τ is the single relaxation time. The viscosity in the LBM model is given by

$$\nu = (\tau - \frac{1}{2})c_s^2\delta t, \tag{6}$$

where $c_s = c/\sqrt{3}$ is the lattice sound speed, and $c = \delta x/\delta t$ is the ratio of lattice spacing δx and time step δt. The equilibrium distribution function $f_\alpha^{eq}(\boldsymbol{x},t)$ can be calculated from

$$f_\alpha^{eq} = \rho w_\alpha[1 + \frac{\boldsymbol{e}_\alpha\cdot\boldsymbol{u}^{eq}}{c_s^2} + \frac{(\boldsymbol{e}_\alpha\cdot\boldsymbol{u}^{eq})^2}{2c_s^4} - \frac{\boldsymbol{u}^{eq}}{2c_s^2}], \tag{7}$$

where w_α is the weighting factor. In this paper, the D3Q19 model is adopted for the 3-dimensional simulations. The weighting factor and discrete velocity for D3Q19 are given by

$$\left[\boldsymbol{e}_0, \boldsymbol{e}_1, \boldsymbol{e}_2, \boldsymbol{e}_3, \boldsymbol{e}_4, \boldsymbol{e}_5, \boldsymbol{e}_6, \boldsymbol{e}_7, \boldsymbol{e}_8, \boldsymbol{e}_9, \boldsymbol{e}_{10}, \boldsymbol{e}_{11}, \boldsymbol{e}_{12}, \boldsymbol{e}_{13}, \boldsymbol{e}_{14}, \boldsymbol{e}_{15}, \boldsymbol{e}_{16}, \boldsymbol{e}_{17}, \boldsymbol{e}_{18} \right] =$$

$$\begin{bmatrix} 0 & 1 & -1 & 0 & 0 & 0 & 0 & 1 & 1 & -1 & -1 & 1 & -1 & 1 & -1 & 0 & 0 & 0 & 0 \\ 0 & 0 & 0 & 1 & -1 & 0 & 0 & 1 & -1 & 1 & -1 & 0 & 0 & 0 & 0 & 1 & 1 & -1 & -1 \\ 0 & 0 & 0 & 0 & 0 & 1 & -1 & 0 & 0 & 0 & 0 & 1 & 1 & -1 & -1 & 1 & -1 & 1 & -1 \end{bmatrix}, \tag{8}$$

$$w_\alpha = \begin{cases} 1/3, & \alpha = 0; \\ 1/18, & \alpha = 1, 2, \ldots, 6; \\ 1/36, & \alpha = 7, 8, \ldots, 18; \end{cases} \tag{9}$$

The local density and local momentum are given by

$$\rho(\boldsymbol{x}, t) = \sum_{\alpha=0}^{N} f_\alpha(\boldsymbol{x}, t), \tag{10}$$

and

$$\rho \boldsymbol{u}(\boldsymbol{x}, t) = \sum_{\alpha=0}^{N} \boldsymbol{e}_\alpha f_\alpha(\boldsymbol{x}, t). \tag{11}$$

The equilibrium value of the velocity $\boldsymbol{u}^{eq}$ used in eq. (7) is given by

$$\boldsymbol{u}^{eq} = \boldsymbol{u} + \frac{\tau \boldsymbol{F}_{total}}{\rho(\boldsymbol{x})}. \tag{12}$$

In eq. (12), $\boldsymbol{F}_{total} = \boldsymbol{F}_{cohesion} + \boldsymbol{F}_{adhesion} + \boldsymbol{F}_{body}$ is the total force on each particle, here including the fluid-fluid cohesion force $\boldsymbol{F}_{cohesion}$, the fluid-solid adhesion force $\boldsymbol{F}_{adhesion}$ and the body force $\boldsymbol{F}_{body}$.

2.2 Fluid-fluid cohesion

It is commonly accepted that the segregation of different phases is microscopically due to the long-range interaction force between the particles at site $\boldsymbol{x}$ and the particles at neighbor sites $\boldsymbol{x}'$ [25]. The interaction force is defined as

$$\boldsymbol{F}_{cohesion}(\boldsymbol{x}) = -\psi(\boldsymbol{x}) \sum_{\boldsymbol{x}'} G(\boldsymbol{x}, \boldsymbol{x}')\psi(\boldsymbol{x}')(\boldsymbol{x}' - \boldsymbol{x}), \tag{13}$$

where $G(\boldsymbol{x}, \boldsymbol{x}')$ is Green's function and satisfies $G(\boldsymbol{x}, \boldsymbol{x}') = G(\boldsymbol{x}', \boldsymbol{x})$. It reflects the intensity of the interparticle interactions and is given by

$$G(\boldsymbol{x}, \boldsymbol{x}') = \begin{cases} g, & |\boldsymbol{x} - \boldsymbol{x}'| = 1, \\ g/2, & |\boldsymbol{x} - \boldsymbol{x}'| = \sqrt{2}, \\ 0, & otherwise. \end{cases} \tag{14}$$

In eq. (13), $\psi(\boldsymbol{x})$ is the effective mass, which is a function of the local density and can be varied to reflect different fluid and fluid mixture behaviors, as represented by various equations. The equation of state (EOS) of the system is given by

$$p = c_s^2 \rho + \frac{c_0}{2} g[\psi(\rho)]^2. \tag{15}$$

and the effective mass can be defined as:

$$\psi(\rho) = \sqrt{\frac{2(p - c_s^2\rho)}{c_0 g}}, \tag{16}$$

where c_0=6.0 for the D3Q19, and p is the pressure. In Yuan and Schaefer's study [26], five different EOS were compared, and it was found that Peng-Robinson (P-R) EOS provided the maximum density ratio while maintaining small spurious currents around the interface. Hence, the P-R EOS was adopted in our following multi-phase flow research, and can be expressed as:

$$p = \frac{\rho RT}{1 - b\rho} - \frac{a\alpha(T)\rho^2}{1 + 2b\rho - b^2\rho^2}, \tag{17}$$

where

$$\alpha(T) = [1 + (0.37464 + 1.5422\omega - 0.26992\omega^2)(1 - \sqrt{T/T_c})]^2. \tag{18}$$

The attraction parameter $a = 0.45724R^2T_c^2/p_c$, the repulsion parameter $b = 0.0778RT_c/p_c$, and ω is the acentric factor. T_c and P_c are the critical temperature and critical pressure respectively. The density ratio and interfacial surface tension are governed by the temperature T, and parameters a and b respectively. Substituting eq. (17) into eq. (16), we get

$$\psi(\rho) = \sqrt{\frac{2(\frac{\rho RT}{1-b\rho} - \frac{a\alpha(T)\rho^2}{1+2b\rho-b^2\rho^2} - c_s^2\rho)}{c_0 g}}. \tag{19}$$

Unlike in the original SC model, the value of the coefficient of interaction strength, g, becomes unimportant. Indeed, it is canceled out when eq. (16) is substituted into eq. (13). The only requirement for g is to ensure that the term inside the square root in eq. (16) is positive, (i.e $g = sgn(p - c_s^2\rho)$ has to be stored when eq.(16) is computed).

2.3 Fluid-solid adhesion and body force

At the fluid-solid interface, the interaction between the fluid and solid needs to be considered. Hence the force applied on a particle that comes in contact with the solid wall is

$$\boldsymbol{F}_{adhesion} = -\rho(\boldsymbol{x}) \sum_{x'} G_w(\boldsymbol{x}, \boldsymbol{x}')\rho_w(\boldsymbol{x}')(\boldsymbol{x}' - \boldsymbol{x}), \tag{20}$$

where $G_w(\boldsymbol{x}, \boldsymbol{x}')$ denotes the intensity of the fluid-solid interaction. For the D3Q19 model, it is defined as

$$G_w(\boldsymbol{x}, \boldsymbol{x}') = \begin{cases} G_w, & |\boldsymbol{x} - \boldsymbol{x}'| = 1, \\ G_w/2, & |\boldsymbol{x} - \boldsymbol{x}'| = \sqrt{2}, \\ 0, & otherwise. \end{cases} \tag{21}$$

Different contact angles can be obtained by adjusting G_w. The term $\rho_w(\boldsymbol{x}')$ in eq. (20) is the wall density, which equals one at the wall and zero in the fluid. In addition to interparticle and wall forces, the body force can be simply defined as

$$\boldsymbol{F}_{body}(\boldsymbol{x}) = \rho(\boldsymbol{x})\boldsymbol{g}. \tag{22}$$

3 Results and discussion

3.1 Impingement of a liquid droplet on flat surface

3.1.1 Initial and boundary conditions

The 3-dimensional computational domain used in the simulations is shown in fig.1. The domain size is 150*150*120 lattice nodes. Periodic boundary conditions are used on the sides of the domain. That means that the particles leaving the domain through a bounding face, will immediately reenter the simulation region through the opposite face. No-slip wall boundary conditions are used on the top and bottom boundaries of the domain, while the half-way bounce-back scheme in LBM is applied on the wall boundary. The domain size for each case is varied according to the initial size of the droplet while the impact is assumed to be isothermal. By varying G_w, the wettability of the flat surface can be controlled. The liquid-gas density ratio is determined by T in eq. (17). In addition, the temperature T and other parameters (a,b) in eq. (17) control the interfacial surface tension between the two fluids. The acentric factor ω is set to be 0.344 in this simulation. Initially, the droplet is placed at the center of the computational domain and is equilibrated for 10000 lattice time steps, after which it is allowed to move towards the

flat surface with a uniform initial velocity $\boldsymbol{U_0}$.

3.1.2 Spreading of the liquid droplet

The snapshots of the different stages of the impact of the liquid drop on the solid flat surface are presented in fig. 2. The simulation parameters are We=52, Re=41, density ratio ρ_l/ρ_g=240, and equilibrium contact angle $\theta_{eq} = 96°$. The evolution time t is non-dimensionalized as $t^\star = tU_0/D_0$, where D_0 is the initial drop diameter and t is the time steps elapsed after the drop comes in contact with the flat surface. Immediately after the impact, the shape of the drop resembles a truncated sphere ($t^\star = 0.2125$). As the droplet impact progresses, a lamella is formed due to the inertial force ($t^\star = 0.4625$). The lamella continues to expand radially while its thickness decreases ($t^\star = 1.8375$). The lamella begins to retract due to gas-liquid interfacial surface tension ($t^\star = 3.3375$ and $t^\star = 6.3375$) after reaching its maximum spread. An equilibrium shape is reached after a couple of oscillations involving spread and recoil ($t^\star = 22.0875$). The time evolution of the spread factor, which is divided into four phases is shown in fig. 3. The four phases include: the kinematic phase, the spreading phase, the relaxation phase and the equilibrium phase [3].

It has been previously investigated through numerical analysis [17] and experimental work [3] that the spread factor is proportional to $\sqrt{t^\star}$ in the kinematic phase. The correlation factor is 2.8 from the experimental data by Rioboo et al. [3], while it equals to 1.35 in the work of Gupta and Kumar [17]. According to the theoretical analysis the correlation factor equals to 2. Fig. 4 shows the time evolution of the spread factor $D^\star$ in the kinematic phase ($t^\star << 1$) for six different We and Re cases using the current LBM model. The Weber number, Reynolds number, density ratio and wettability of the surface for these six cases are illustrated in table 1. A fitting curve has been generated to yield $D^\star = 2\sqrt{t^\star}$ which is the same as the theoretical result. It can be observed from fig. 4 that all cases behave similarly during the kinematic phase. Therefore, the droplet spread factor in the kinematic phase is independent of the the physical properties of the

fluids and the wettability of the surface, while it is only a function of the dimensionless time.

The maximum spread factor is obtained at the end of the spreading phase, which follows the kinematic phase. It depends on the capillary force, viscosity and inertial effects as well as the contact angle. Asai et al. [4] proposed a correlation for the maximum spread factor which is given by

$$D^{\star}_{max} = 1 + 0.48We^{0.5}exp[-1.48We^{0.22}Re^{-0.21}]. \tag{23}$$

Another maximum spread factor prediction equation was derived based on the energy conservation equation and the viscous dissipation based on the linear velocity profile [6]

$$\frac{3}{2}\frac{We}{Re}{D^{\star}_{max}}^{4} + (1 - cos\theta_w){D^{\star}_{max}}^{2} - (\frac{We}{3} + 4) = 0. \tag{24}$$

The maximum spread factor prediction equation from Pasandideh-Fard et al. [7] is also based on energy conservation equation, while the viscous dissipation was based on the velocity profile of stagnation-point flow.

$$D^{\star}_{max} = \sqrt{(We + 12)/[3(1 - cos\theta_w) + 4We/\sqrt{Re}]}. \tag{25}$$

In order to cover a large range of We and Oh numbers, Mao et al. [8] proposed an empirical equation based on the energy conservation equation

$$[0.2Oh^{0.33}We^{0.665} + \frac{1}{4}(1 - cos\theta_w)]{D^{\star}_{max}}^{2} + \frac{2}{3}{D^{\star}_{max}}^{-1} = \frac{We}{12} + 1. \tag{26}$$

Scheller and Bousfield [5] generated a experimental equation to predict $D^{\star}_{max}$ given by

$$D^{\star}_{max} = 0.61(Re^2Oh)^{0.166}. \tag{27}$$

Although the effect of the equilibrium contact angle was neglected, the empirical equation was in good agreement with Dong et al.'s [10] experiment. The maximum spread factor predicted from our simulation results is compared with previous studies [4–8] in fig. 5. It can be observed that the simulation results are in good agreement with the predictions from the equations of Asai et al. [4] and Mao et al. [8]. A good correlation with the results of Chandra and Avedisians' [6] is also observed, especially at higher $OhRe^2$ numbers, while minor deviations are present at lower $OhRe^2$ numbers. Discrepancies can be seen between the numerical results and the predictions from Pasandideh-Fard et al. [7], while the correlation of Scheller and Bousfield significantly under predicts $D^{\star}_{max}$ especially for low $OhRe^2$ numbers. These discrepancies can mainly be attributed to the fact that Pasandideh-Fard et al's. [7] evaluation of dissipation is suitable for low Oh numbers, while Chandra and Avedisian' [6] dissipation evaluation becomes more suitable for high Oh numbers. This has also been pointed out in the work of Mao et al. [8].

Simulations were conducted for a range of Weber and Reynolds numbers in this study, while keeping the density ratio between liquid and gas, the wettability of the surface and the Ohnesorge number (Oh) constant as 240, 96°, and 0.177, respectively. In fig. 6, the time evolution of the droplet spreading process on a dry flat surface for Oh=0.177 is shown. It can be seen that in the kinematic phase, $D^{\star}$ is proportional to $\sqrt{t^{\star}}$ for all Reynolds numbers. The spreading phase depends on the Weber and Reynolds numbers, which control both the maximum diameter and the time to achieve it. Increasing the inertial force leads to an increase in the maximum spread factor. For the lowest Reynolds number of 18.72, the maximum spread factor is 1.43, while the maximum value is 1.72 when the Reynolds number is 41. Another observation from fig. 6 is that longer times are needed for the droplets to reach the peak diameter and the equilibrium shape as the Weber number and Reynolds number increase. The influence of the surface tension on the spreading process is estimated by varying the Weber number while keeping the Reynolds number and equilibrium contact angle at a constant value of 31.2 and 96°, respectively. From fig. 7, the maximum spread factor is 1.61 at We=30.72 and the maximum value

is 1.58 when We=16. Hence, the influence of surface tension on the maximum spread factor is weak and the maximum spread factor mainly depends on the Reynolds number. The effect of the wettability of the flat surface on the spread factor is plotted in fig. 8. Three different surfaces have been used: hydrophilic, neutral, and hydrophobic with static contact angles of $\theta_w = 76°$, $\theta_w = 91°$, $\theta_w = 104°$, respectively. It can be seen that the influence of θ_w becomes significant during the relaxation phase. For $\theta_w = 104°$, secondary spreading and oscillation are observed, but not for the case where $\theta_w = 76°$. The recoil speed is slower for low θ_w, and as θ_w decreases, the equilibrium spread factor and maximum spread factor increase.

3.2 Impingement of a liquid droplet on a sphere

3.2.1 Initial and boundary conditions

The 3-dimensional computational domain used for the simulation of the droplet impact onto a spherical target is shown in fig. 9. The domain size is 150*150*180 lattice nodes. No-slip wall boundary conditions were used on the sphere's surface and periodic boundary conditions were used on all sides of the domain. The methods that control the wettability of the sphere's surface, density ratio and interfacial surface tension are the same with the ones used in the simulation of the droplet impingement on a flat surface. Initially, the droplet is located several nodes away from the sphere, where it is equilibrated for 5000 lattice time steps. After equilibration, the droplet is released towards the spherical target with initial velocity U_0. According to the experimental study of Bakshi et al. [13], the dynamics of the film flow on the surface of the sphere is influenced by two non-dimensional parameters which are the droplet Reynolds number and the target-to-drop size ratio, where the latter is defined as $R^\star = 2R_s/D_0$.

3.2.2 Dynamics of the film flow on the surface of sphere

Figs. 10 and 11 show a sequence of the cross-sectional view and the 3-dimensional view of the impact of the droplet onto a solid curved surface with Re=42.48, We=26.14 (a=1, b=2), density ratio ρ_l/ρ_g=328, gravity is equal to 0.00005 in lattice units and equilibrium contact angle 76°. In fig. 10, the formation of the liquid lamella around the surface of the target is clearly observed. The initial drop deformation period is similar to the first phase of the droplet impact onto the flat surface. The bottom part of the droplet is deformed as it comes in contact with the target($t^\star = 0.0407$ and $t^\star = 0.0814$), while the top part remains spherical under the action of the surface tension. The liquid lamella appears around the surface of the sphere with the liquid continuing to flow downwards ($t^\star = 0.6102$ and $t^\star = 1.2203$) and reaching its maximum spreading at $t^\star = 2.0339$. Following that, the thickness of the lamella slowly decreases governed by surface tension, viscous and gravitational forces ($t^\star = 10.1695$). The corresponding temporal variation of the film thickness at the north pole of the spherical target is shown in fig. 12 in a log-log plot. The film thickness is nondimensionalized with the initial droplet diameter as $h^\star = h/D_0$. The non-dimensional time $t^\star$=0 corresponds to the instant of the initial contact of the drop with the sphere. In this case, the target-to-drop size ratio $R^\star$ is 1.23. Three distinct temporal phases of the film dynamics can be clearly observed in fig. 12. The first phase is the droplet deformation period in which the upper part of the droplet continues to move at the impacting velocity. The non-dimensional film thickness and time satisfy the equation $h^\star = 1 - t^\star$ in this phase. During the second phase, inertial forces dominate the viscous forces and surface tension, thus the temporal variation is given by the equation $h^\star = 0.15/t^{\star 2}$ for $R^\star = 1.23$ from the experimental study of Bakshi et al. [13]. In our simulation, a fitting curve is generated which yields $h^\star = 0.185/t^{\star 1.6}$. The difference might be due to the influence of other parameters such as wettability and Bond number ($Bo = \rho_l g D_0/\sigma$). From the physical point of view, the inertial forces dominate the viscous, gravitational and surface tension forces at the early stages of the second phase. The influence of gravity and surface tension becomes noticeable during the

late stages of the second phase and throughout the third phase, where the initial kinetic energy has been dissipated. Hence, the variation in the wettability of the surface which is associated with the surface tension effects, as well as the presence of the gravitational acceleration can significantly influence the rate of reduction of the film thickness. During the third phase, the film thickness almost reaches a residual value and decreases slowly due to the balance of surface tension, viscous forces and gravity.

Simulations have been performed for different values of droplet Reynolds number with the same target-to-drop size ratio, wettability and Bond number, in order to evaluate its effect on the dynamics of the film flow on the surface of the sphere. Fig. 13 shows the time evolution of the film thickness at the north pole of the target for different Reynolds numbers. From fig. 13, the following observation can be made, a) the non-dimensional temporal variation of film thickness for different values of Reynolds number collapses onto a single curve in the first and second phases; b) the transition to the third phase occurs earlier for the low Reynolds numbers; c) the residual thickness in the third phase decreases with increasing Reynolds number; d) an additional phase appears between second and third phase in the case of low Reynolds numbers. This recoil process is due to the surface tension action. All of the previously mentioned observations are in line with the experimental results of Bakshi et al. [13]. However, the Reynolds number is varied by changing the impact velocity keeping the kinematic viscosity constant in the experimental research of Bakshi et al. [13]. The Weber number is also varied during this process. In order to check the effects of the Reynolds number and Weber number individually, different Reynolds numbers are obtained by altering the kinematic viscosity and different Weber numbers are obtained by varying the surface tension. Fig. 14 shows the time evolution of the film thickness at the north pole of the target for different Reynolds numbers by adjusting the kinematic viscosity, while the Weber number is invariable. In order to avoid the effect of gravity, the gravity force is not included into this case. From fig. 14, it can be seen that the temporal variation of the film thickness still collapses onto a single curve at the first half of the second phase. This is because the inertial force

dominates the viscous force during the first half of the second phase. As the initial kinetic energy of the droplet is dissipated by the viscous forces and on the surface energy, the influence of the viscous force becomes obvious at the end of the second phase. Also the decrease rate of the film thickness becomes slower with increasing kinematic viscosity at the end of the second phase. From a physical point of view, when the kinematic viscosity is increased, the influence of the viscous force in the second phase will appear earlier. In this case, the film thickness does not collapse onto a single curve in the second phase. However, due to the restrictions of the current LBM model, τ cannot take values less than one, so the variation of the kinematic viscosity is limited in a narrow range. Fig. 15 shows the effects of the surface tension on the dynamics of the film flow process. Simulations were conducted for different values of Weber number while the Reynolds number was held constant. The parameters a=1/49 and b=2/21 for the high Weber number case, while a=2/49 and b=2/21 for the low Weber number case. The gravity force is ignored in this case. From fig. 15, it can be observed that the effect of surface tension can be neglected in the first and second phases, thus the rate of film thickness reduction is the same. However, the surface tension dominates the inertial force at the end of the second phase and the transition to the retraction phase occurs earlier for the low Weber number case.

The influence of the target-to-drop size ratio on the dynamics of film flow has also been investigated. Fig. 16 shows the time evolution of the film thickness at the north pole of the solid sphere for different values of target-to-drop size ratios, for the same value of droplet Reynolds number, Weber number, wettability and Bond number. The solid line ($R^\star = 0$) in fig. 16, represents the free fall of the droplet with an impacting velocity which corresponds to the case of the zero target-to-drop size ratio. The case of the largest target-to-drop size, which corresponds to the droplet impact on a flat surface is represented by the dashed line ($R^\star$ is largest). As seen in fig. 16, the rate of film thickness reduction becomes slower with increasing target-to-drop ratio, $R^\star$. Hence, the increase of the target size has an inverse effect on the rate at which the film thickness reduction occurs. The

residual film thickness also increases with increasing target-to-drop size ratio, something that has the same effect as decreasing the Reynolds number. The simulation parameters for all test cases are summarised in table 2.

4 Conclusions

In the present work, the liquid droplet impact on a flat surface and a solid sphere has been simulated by a 3-dimensional lattice Boltzmann model which can tolerate high density ratios. It has been shown that there are four phases during the droplet impact on flat surface which include: the kinematic phase, the spreading phase, the relaxation phase and the equilibrium phase. In the kinematic phase, the droplet spread factor does not depend on the physical properties of the fluids and surface wettability, and it is only a function of the non-dimensional time ($D^\star = 2\sqrt{t^\star}$). In the spreading phase, it is shown that increasing the inertia leads to an increase in the maximum spread factor.

For given Oh, it can be seen that inertia controls the maximum diameter as well as the time needed to reach the peak diameter in the spreading phase. Longer times are needed to reach the equilibrium shape for high Weber and Reynolds numbers. It is also found that the influence of surface tension on the maximum spread factor is weak, while the influence of the wettability of the surface becomes significant during the relaxation phase. The secondary spread and oscillation appear for higher θ_w, while they are absent for low θ_w under the same Reynolds and Weber numbers. As the contact angle decreases, the equilibrium spread factor and maximum spread factor increase, while the recoil speed becomes slower.

The investigation of film flow on the curved surface is also included in this study. In the first phase, the non-dimensional film thickness follows the correlation given by $h^\star = 1 - t^\star$. Inertia dominates the viscous forces during the second phase, while the non-dimensional time and film thickness satisfy the relation $h^\star = 0.185/t^{\star 1.6}$ for the $R^\star = 1.23$ case. The film thickness almost reaches a residual value in the third phase which is governed by the

balance of gravity, viscous forces and surface tension.

Simulations were also performed with various droplet Reynolds numbers and target-to-drop size ratios to evaluate the effect of these parameters on the dynamics of the film flow on the surface of the sphere. From the simulation results, the following conclusions can be obtained, a) the non-dimensional time and film thickness curve for different values of Reynolds number collapses onto a single curve in the first and second phases when the Reynolds number is controlled by the impact velocity; b) the influence of the viscous forces will appear at the end of the second phase and the rate of film thickness decrease becomes slower with increasing kinematic viscosity when the Reynolds number is controlled by varying the kinematic viscosity; c) the effect of surface tension can be neglected at the first and second phases, while the surface tension dominates the inertial force at the end of the second phase and the transition to the retraction phase occurs earlier for the low Weber number case; d) the rate of film thickness reduction becomes slower with increasing target-to-drop ratio.

It was shown that lattice-Boltzmann modelling can provide a significant insight on the physical phenomena that govern the droplet impact process. Follow-up development will include the incorporation of a multi-relaxation time lattice-Boltzmann model, in order to investigate the effects of low viscosity, and consequently higher Reynolds numbers, on the droplet impact and film flow dynamics on the target surfaces.

References

[1] A.L.Yarin, Drop impact dynamics: Splashing, spreading, receding, bouncing..., Annu. Rev. Fluid Mech. 38(2006) 159-192.

[2] M.Rein, Phenomena of liquid drop impact on solid and liquid surface, Fluid. Dyn. Res. 12(1993) 61-93.

[3] R.Rioboo, M.Marengo, C.Tropea, Time evolution of liquid drop impact onto solid, dry surfaces, Exp. Fluids. 33(2002) 112-124.

[4] A.Asai, M.Shioya, S.Hirasawa, T.Okazaki, Impact of an ink drop on paper, J Imaging Sci Techn. 37(1993) 205-207.

[5] B.L.Scheller, D.W.Bousfield, Newtonian drop impact with a solid surface, AIChE J. 41(1995) 1357-1367.

[6] S. Chandra and C. T. Avedesian, On the collision of a droplet with a solid surface, Proc. R. Soc. London, Ser. A 432(1991) 13.

[7] M.Pasandideh-Fard, Y.M.Qiao, S.Chandra, J.Mostaghimi, Capillary effects during droplet impact on a solid surface, Phys Fluids. 8(1996) 650-660.

[8] T.Mao, D.C.S.Kuhn, H.Tran, Spread and rebound of liquid droplets upon impact on flat surfaces, AIChE J. 43(1997) 2169-2179.

[9] I.V.Roisman, R.Rioboo, C.Tropea, Normal impact of a liquid drop on a dry surface: Model for spreading and receding, Proc. R. Soc. London, Ser. A 458(2002) 1411-1430.

[10] H.Dong, W.W.Carr, D.G.Bucknall, J.F.Morris, Temporally-resolved inkjet drop impaction on surfaces, AIChE J. 53(2007), 2606-2617.

[11] L.S.Hung, S.C.Yao, Experimental investigation of the impaction of water droplets on cylindrical objects, Int. J. Multiphase Flow 25(1999) 1545-1559.

[12] Y.Hardalupas, A.M.K.P.Taylor, J.H.Wilkins, Experimental investigation of submillimeter droplet impingement onto spherical surfaces, Int. J. Heat Fluid Flow 20 (1999) 477-485.

[13] S.Bakshi, L.V.Roisman, C.Tropea, Investigations on the impact of a drop onto a small spherical target, Phys Fluids. 19(2007) 032102.

[14] S.Mukherjee, Numerical simulation of wall impinging drops, Ph.D.thesis, School of Mechanical Engineering, Purdue University 2006.

[15] G.Trapaga, J.Szekely, Mathematical Modeling of the Isothermal Impingement of Liquid Droplets in Spraying Processes, Metall. Trans. B. 22(1991) 901-914.

[16] M.Bussmann, S.Afkhami, Drop impact simulation with a velocity-dependent contact angle, Chem. Eng. Sci. 62(2007) 7214-7224.

[17] A.Gupta, R.Kumar, Droplet impingement and breakup on a dry surface, Comput. Fluids. 39(2010) 1696-1703.

[18] A.Gupta, R.Kumar, Two-dimensional lattice Boltzmann model for droplet impingement and breakup in ow density ratio liquids, Comm. Comp. Phys. 10(2011) 767-784.

[19] Y.Y.Yan, Y.Q.Zu, A lattice Boltzmann method for incompressible two-phase flows on partial wetting surface with large density ratio, J. Comput. Phys. 227(2007) 763-775.

[20] T.Inamuro, T.Ogata, S.Tajima, N.Konishi, A lattice Boltzmann method for incompressible two-phase flows with large density differences, J. Comput. Phys. 198(2004) 628-644.

[21] A.J.Briant, P.Papatzacos, J.M.Yeomans, Lattice Boltzmann simulations of contact line motion in a liquid-gas system, Philos. Trans. Roy. Soc. Lond. A. 360(2002) 485-495.

[22] A.Fakhari, M.H.Rahimian, Phase-field modeling by the method of lattice Boltzmann equations, Phys. Rev. E. 81(2010) 036707.

[23] M.R.Swift, E.Orlandini, W.R.Osborn, J.M.Yeomans, Lattice Boltzmann simulations of liquid-gas and binary fluid systems, Phys. Rev. E. 54(1996) 5041-5052.

[24] S.Q.Shen, F.F.Bi, Y.L.Guo, Simulation of droplets impact on curved surfaces with lattice Boltzmann method, Int. J. Heat Mass Tranf. 55(2012) 6938-6943.

[25] X.Shan, H.Chen, Simulation of nonideal gases and liquid-gas phase transitions by the lattice Boltzmann equation, Phys. Rev. E. 49(1994) 2941-2948.

[26] P.Yuan, L.Schaefer, Equations of state in a lattice Boltzmann model, Phys Fluids. 18(2006) 042101.

[27] D.H.Rothman, J.M.Keller, Immiscible cellular-automation fluids, J. Statist. Phys. 52(1988) 1119-1129.

[28] X.He, S.Chen, R.Zhang, A lattice Boltzmann scheme for incompressible multiphase flow and its application in simulation of Rayleigh-Taylor instability, J. Comput. Phys. 152(1999) 642-663.

[29] T.Reis, T.N.Phillips, Lattice Boltzmann model for simulating immiscible two-phase flows, J. Phys. A: Math. Theor. 40(2007) 4033-4053.

[30] S.Leclaire, M.Reggio, J.-Y.Trepanier, Numerical evaluation of two recoloring operators for an immiscible two-phase flow lattice Boltzmann model. 36(2012) 2237-2252.

[31] S.Leclaire, P.Nicolas, M.Reggio, J.-Y.Trepanier, Enhanced equilibrium distribution functions for simulationg immiscible multiphase flows with variable density ratios in a class of lattice Boltzmann models. 57(2013) 159-168.

[32] H.B.Huang, H.W.Zheng, X.Y.Lu, C.Shu, An evaluation of a 3D free-energy-based lattice Boltzmann model for multiphase flows with large density ratio, Int. J. Numer. Meth. Fluids. 63(2009) 1193-1207.

[33] T.Lee, C.L.Lin, A stable discretization of the lattice Boltzmann equation for simulation of incompressible two-phase flows at high density ratio, J. Comput. Phys. 206(2005) 16-47.

[34] H.W.Zheng, C.Shu, Y.T.Chew, A lattice Boltzmann model for multiphase flows with large density ratio, J. Comput. Phys. 218(2006) 353-371.

[35] D.A.Perumal, A.K.Dass,Application of lattice Boltzmann method for incompressibe viscous flows, Applied Mathematical Modelling. 37(2013) 4075-4092.

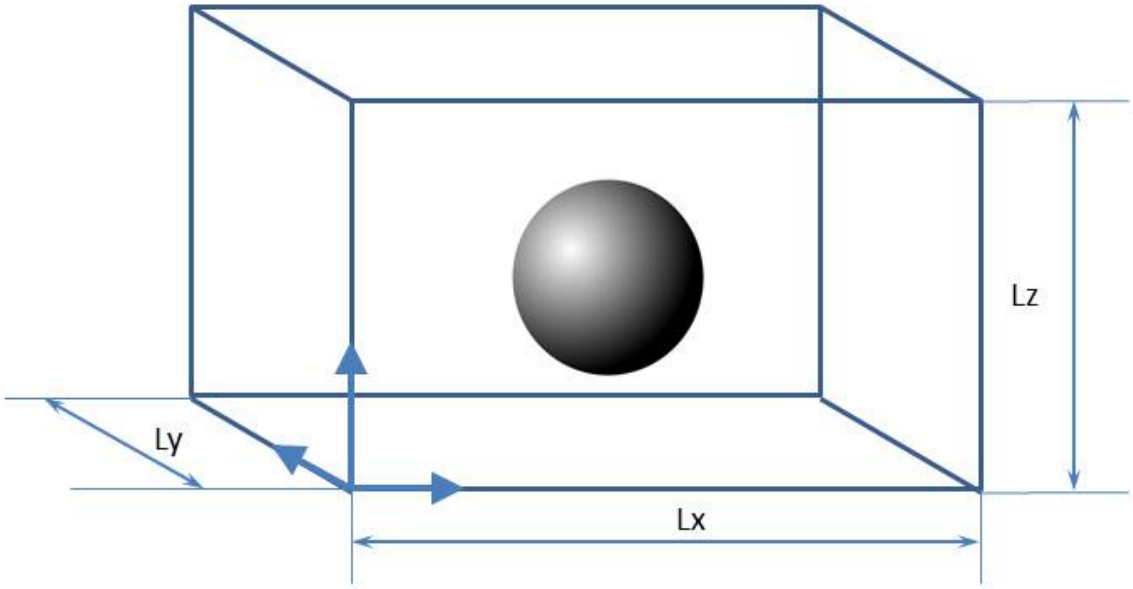
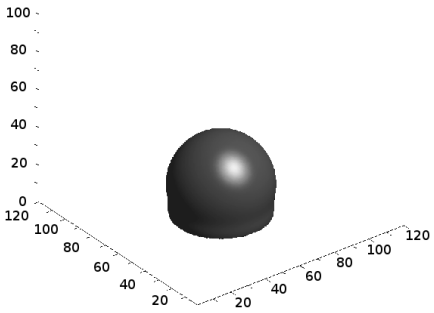
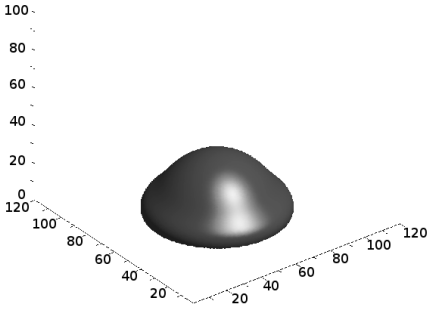


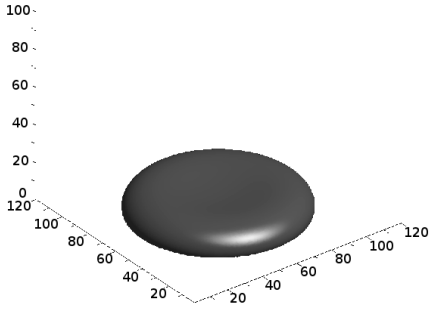
Figure 1



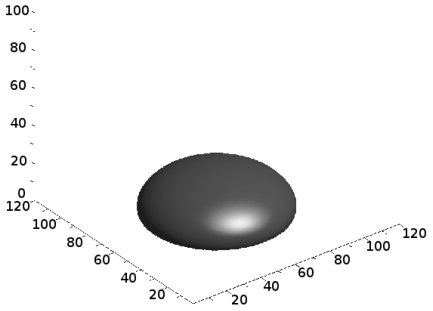
$t^\star = 0.2125$



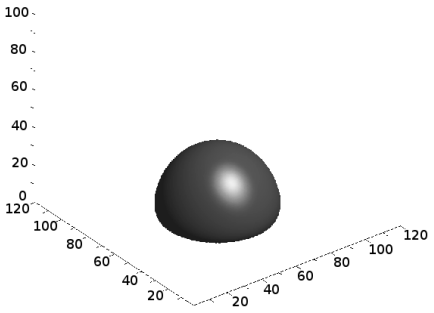
$t^\star = 0.4625$



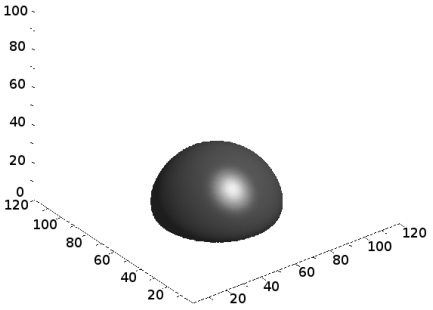
$t^\star = 1.8375$



$t^\star = 3.3375$



$t^\star = 6.3375$



$t^\star = 22.0875$

Figure 2

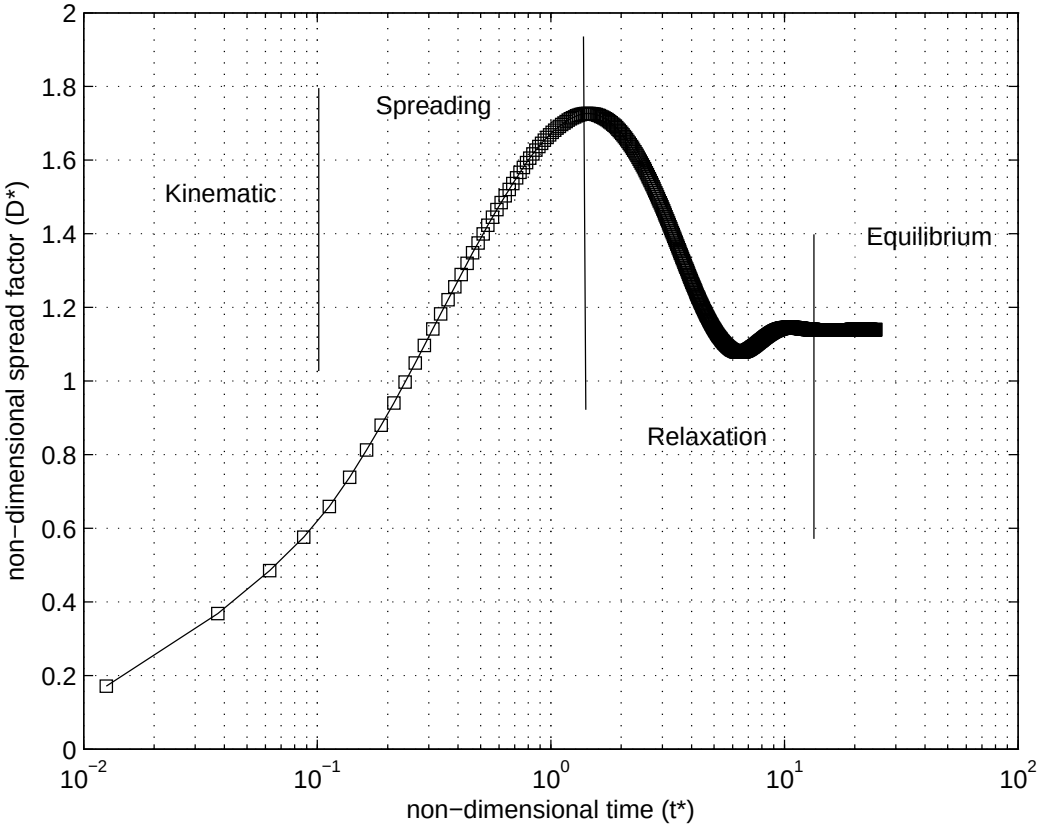

Spreading
Kinematic
Equilibrium
Relaxation
non−dimensional spread factor (D*)
non−dimensional time (t*)
2
1.8
1.6
1.4
1.2
1
0.8
0.6
0.4
0.2
0
10^−2
10^−1
10^0
10^1
10^2

Figure 3

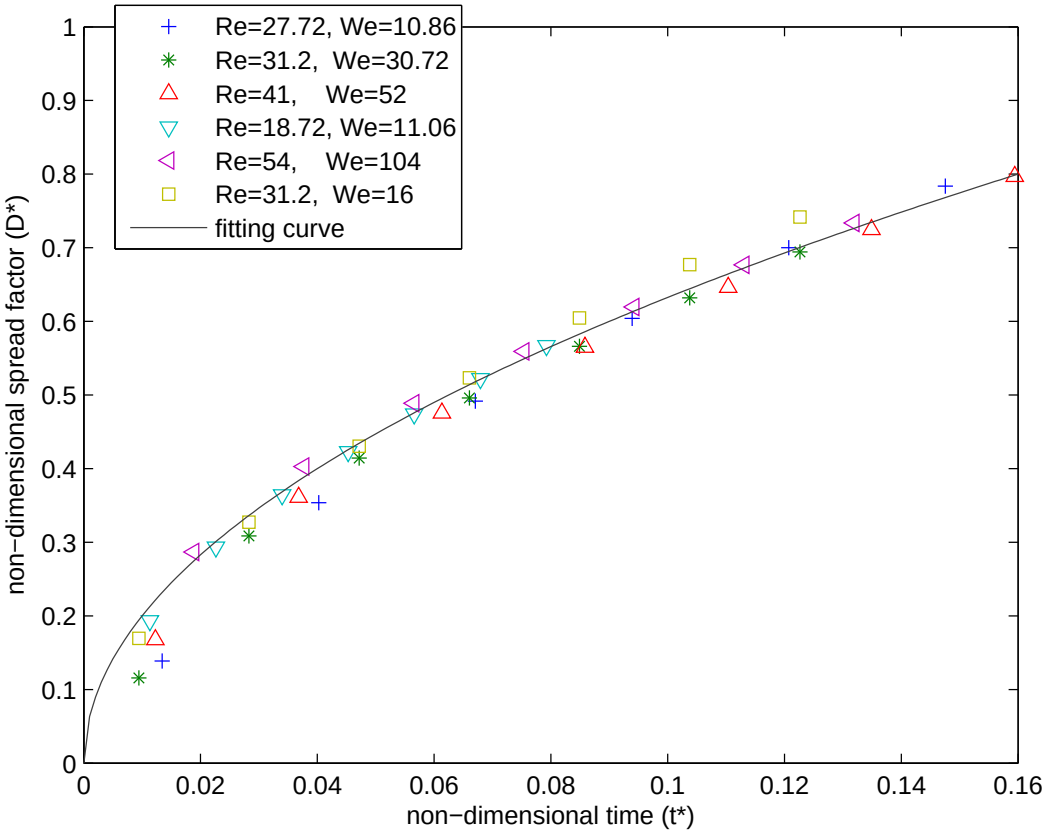

Re=27.72, We=10.86
Re=31.2, We=30.72
Re=41, We=52
Re=18.72, We=11.06
Re=54, We=104
Re=31.2, We=16
fitting curve
non−dimensional spread factor (D*)
non−dimensional time (t*)
0
0.1
0.2
0.3
0.4
0.5
0.6
0.7
0.8
0.9
1
0.02
0.04
0.06
0.08
0.1
0.12
0.14
0.16

Figure 4

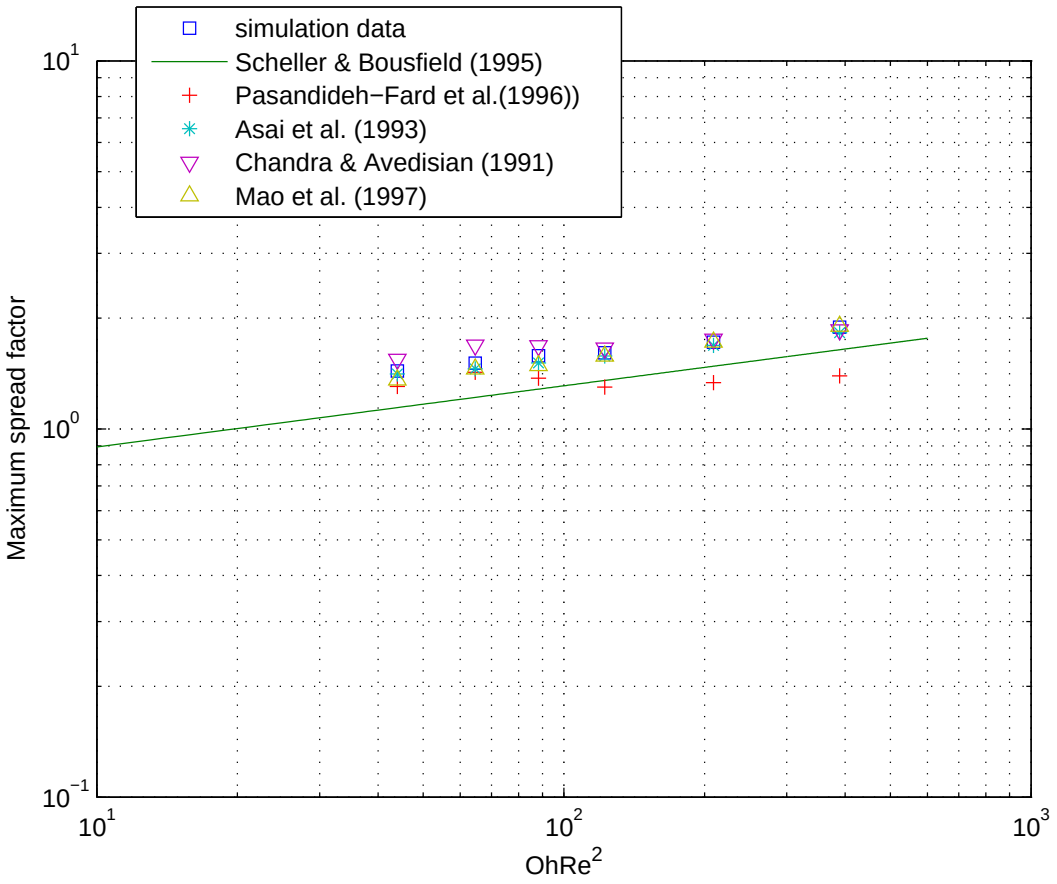

simulation data
Scheller & Bousfield (1995)
Pasandideh−Fard et al.(1996))
Asai et al. (1993)
Chandra & Avedisian (1991)
Mao et al. (1997)
Maximum spread factor
OhRe^2
10^1
10^0
10^{-1}
10^1
10^2
10^3

Figure 5

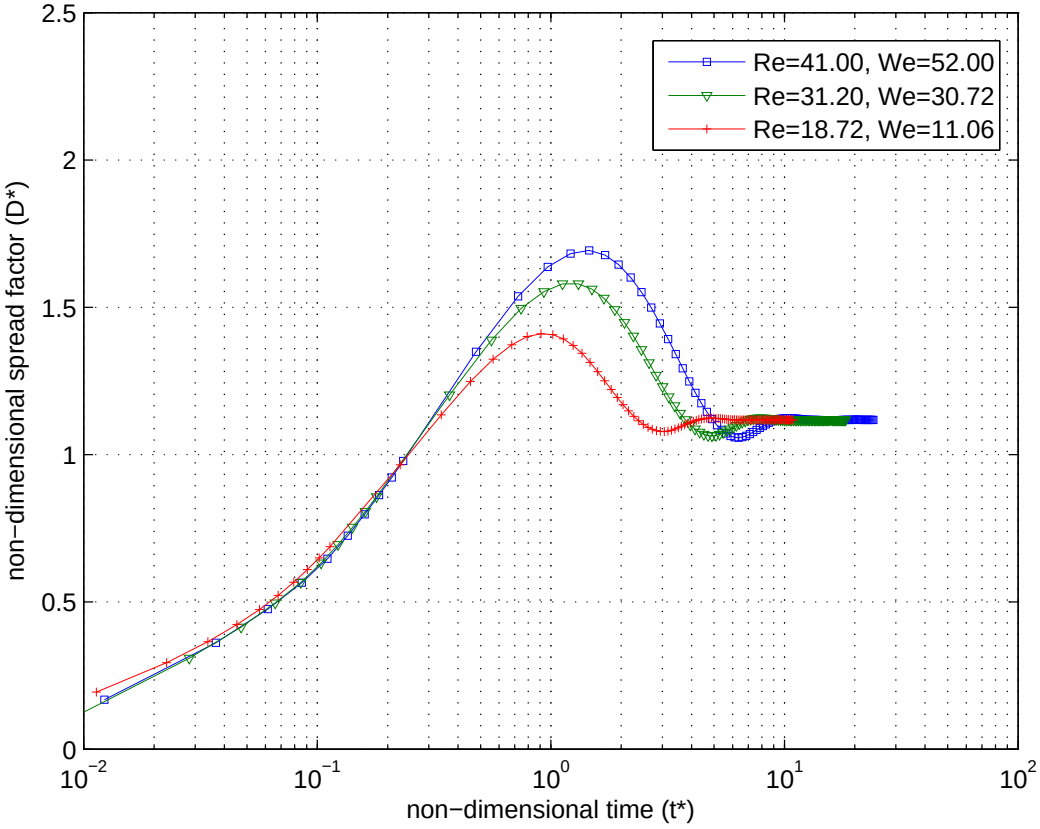

Re=41.00, We=52.00
Re=31.20, We=30.72
Re=18.72, We=11.06
non−dimensional spread factor (D*)
non−dimensional time (t*)
2.5
2
1.5
1
0.5
0
10^−2
10^−1
10^0
10^1
10^2

Figure 6

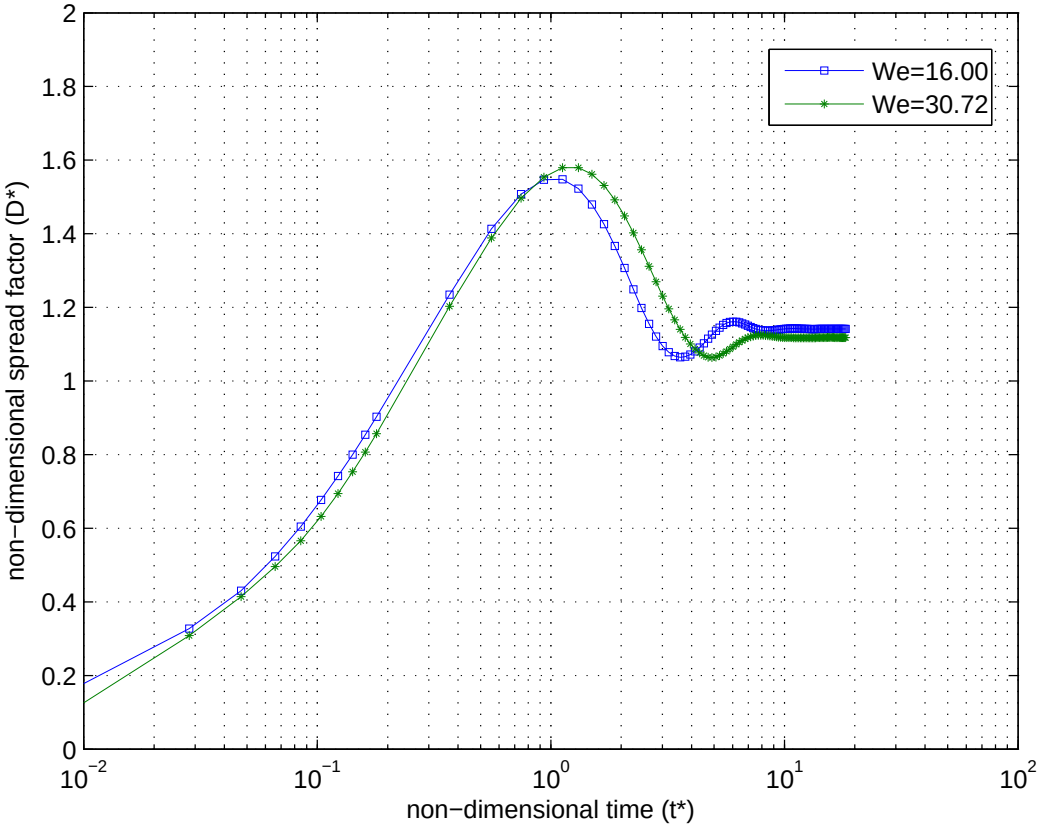

We=16.00
We=30.72
non−dimensional spread factor (D*)
non−dimensional time (t*)
0
0.2
0.4
0.6
0.8
1
1.2
1.4
1.6
1.8
2
10^−2
10^−1
10^0
10^1
10^2

Figure 7

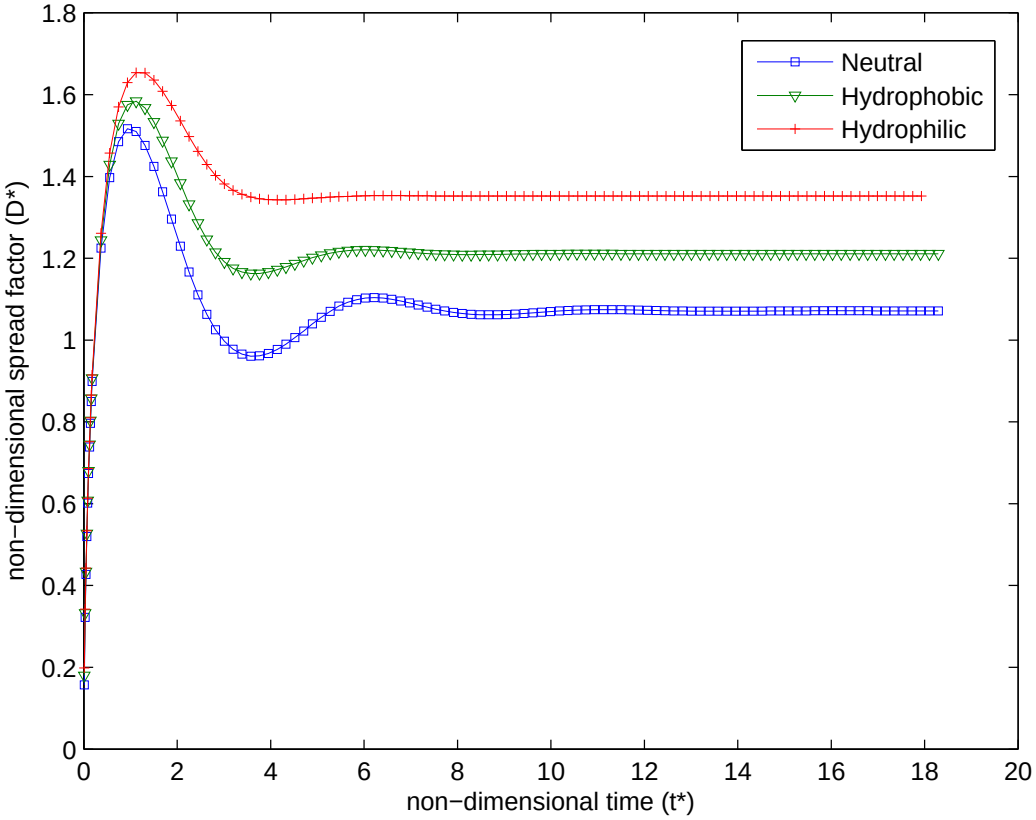

Neutral
Hydrophobic
Hydrophilic
non−dimensional spread factor (D*)
non−dimensional time (t*)
0
0.2
0.4
0.6
0.8
1
1.2
1.4
1.6
1.8
0
2
4
6
8
10
12
14
16
18
20

Figure 8

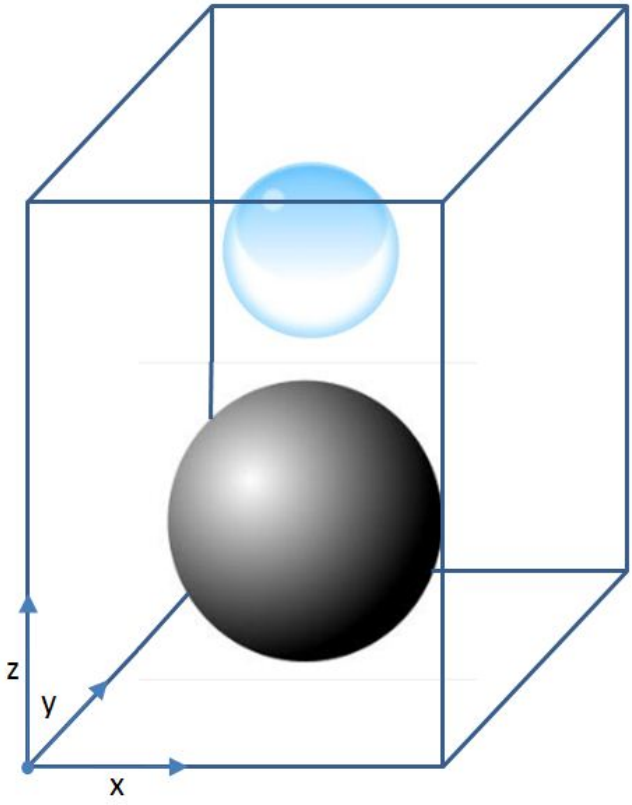


Figure 9

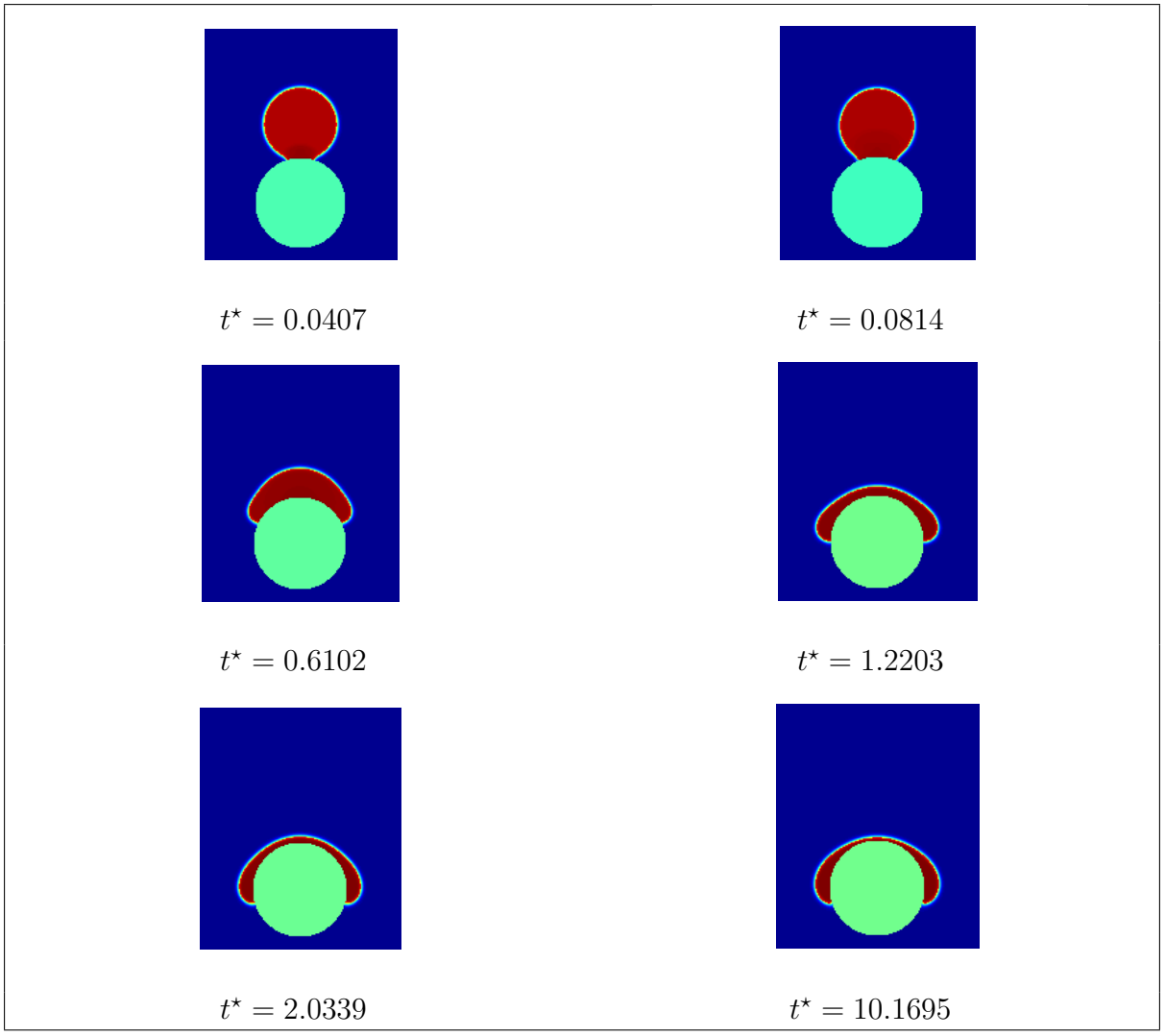

$t^\star = 0.0407$
$t^\star = 0.0814$
$t^\star = 0.6102$
$t^\star = 1.2203$
$t^\star = 2.0339$
$t^\star = 10.1695$

Figure 10

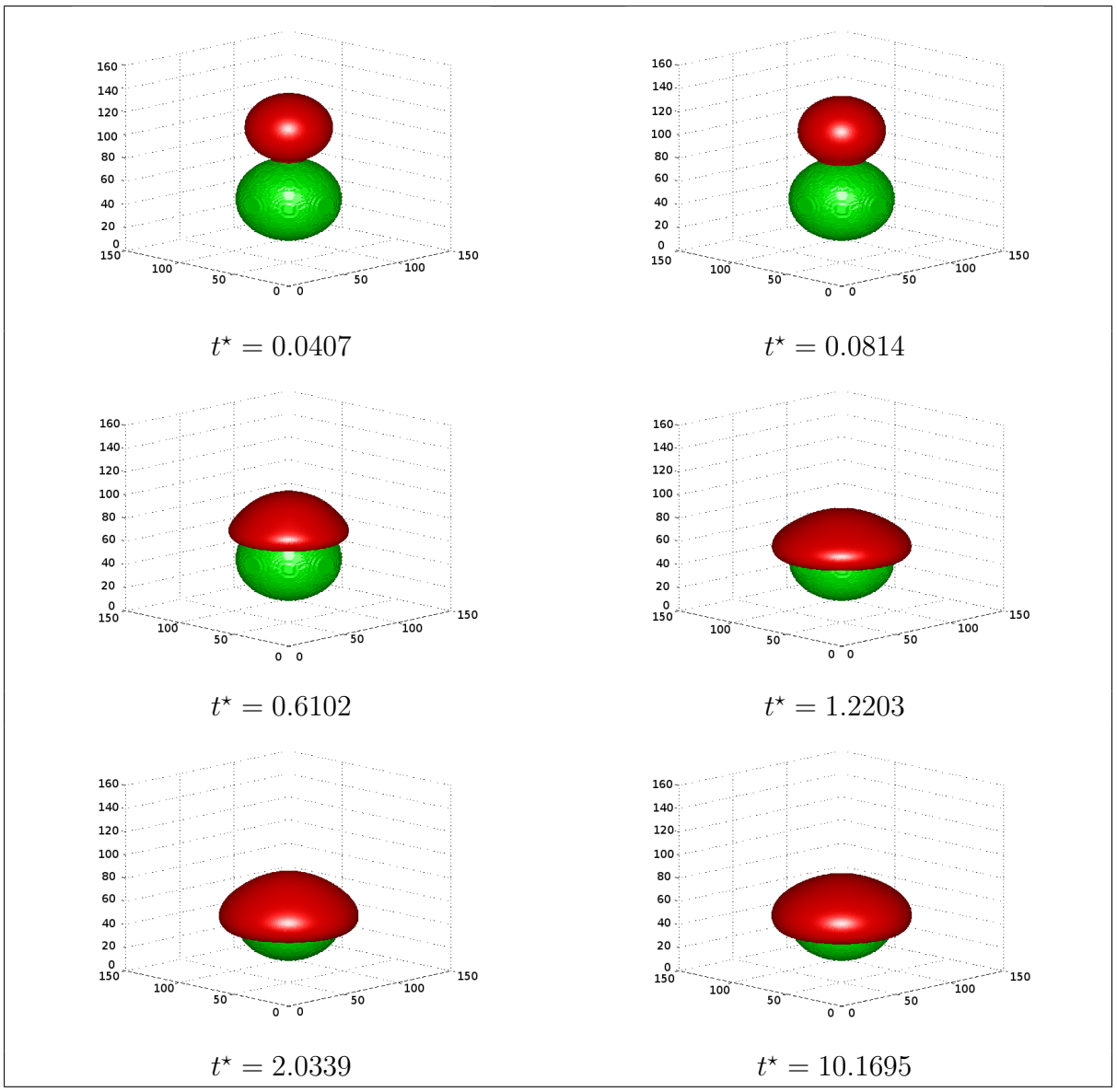

$t^\star = 0.0407$
$t^\star = 0.0814$
$t^\star = 0.6102$
$t^\star = 1.2203$
$t^\star = 2.0339$
$t^\star = 10.1695$

Figure 11

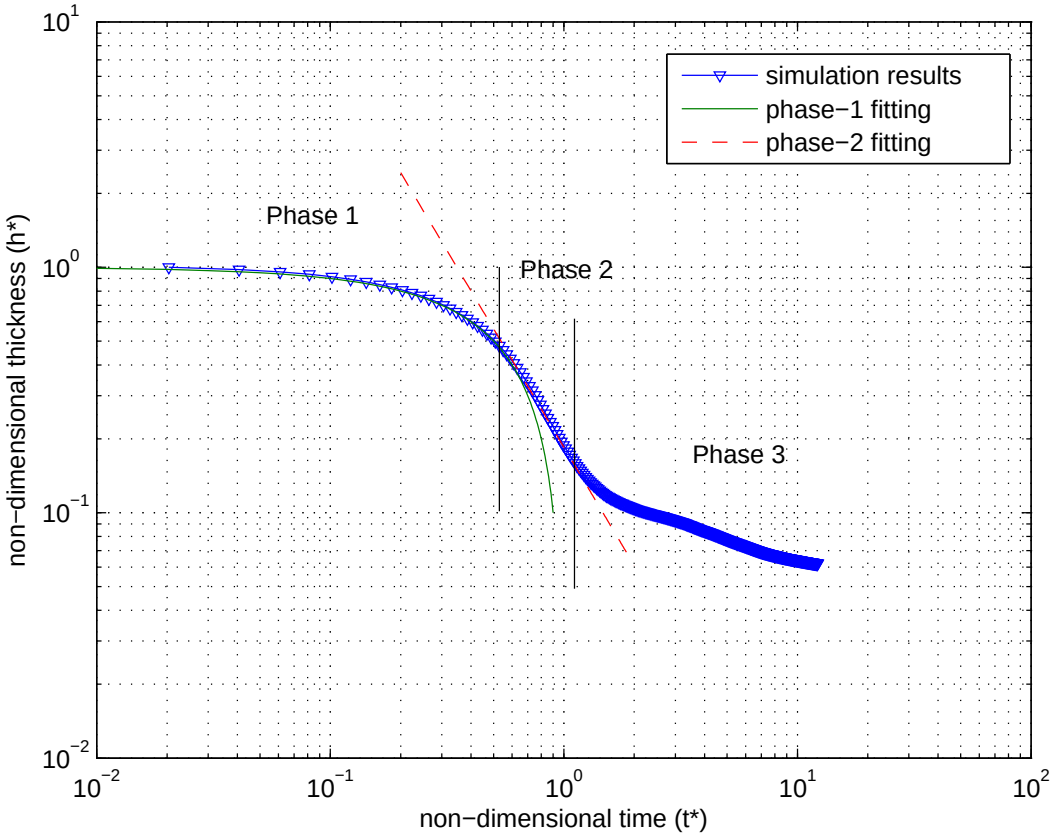

simulation results
phase−1 fitting
phase−2 fitting
Phase 1
Phase 2
Phase 3
non−dimensional thickness (h*)
non−dimensional time (t*)
10^1
10^0
10^−1
10^−2
10^−2
10^−1
10^0
10^1
10^2

Figure 12

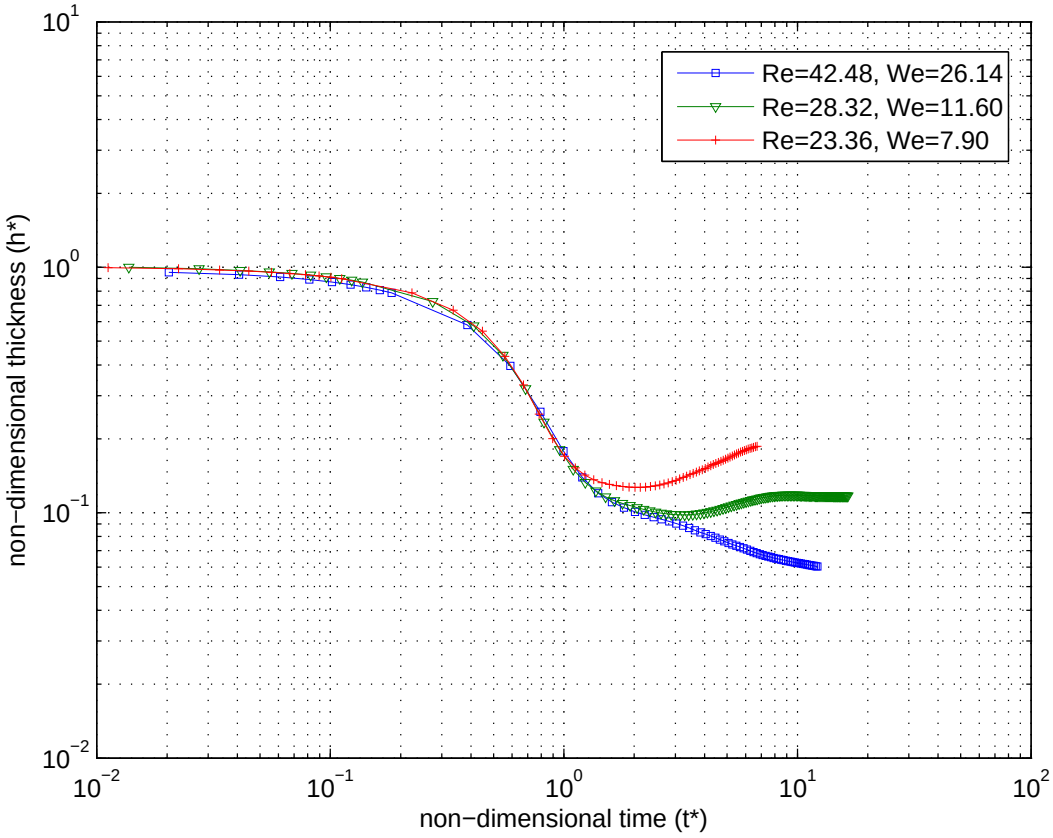

Re=42.48, We=26.14
Re=28.32, We=11.60
Re=23.36, We=7.90
non−dimensional thickness (h*)
non−dimensional time (t*)
10^1
10^0
10^−1
10^−2
10^−2
10^−1
10^0
10^1
10^2

Figure 13

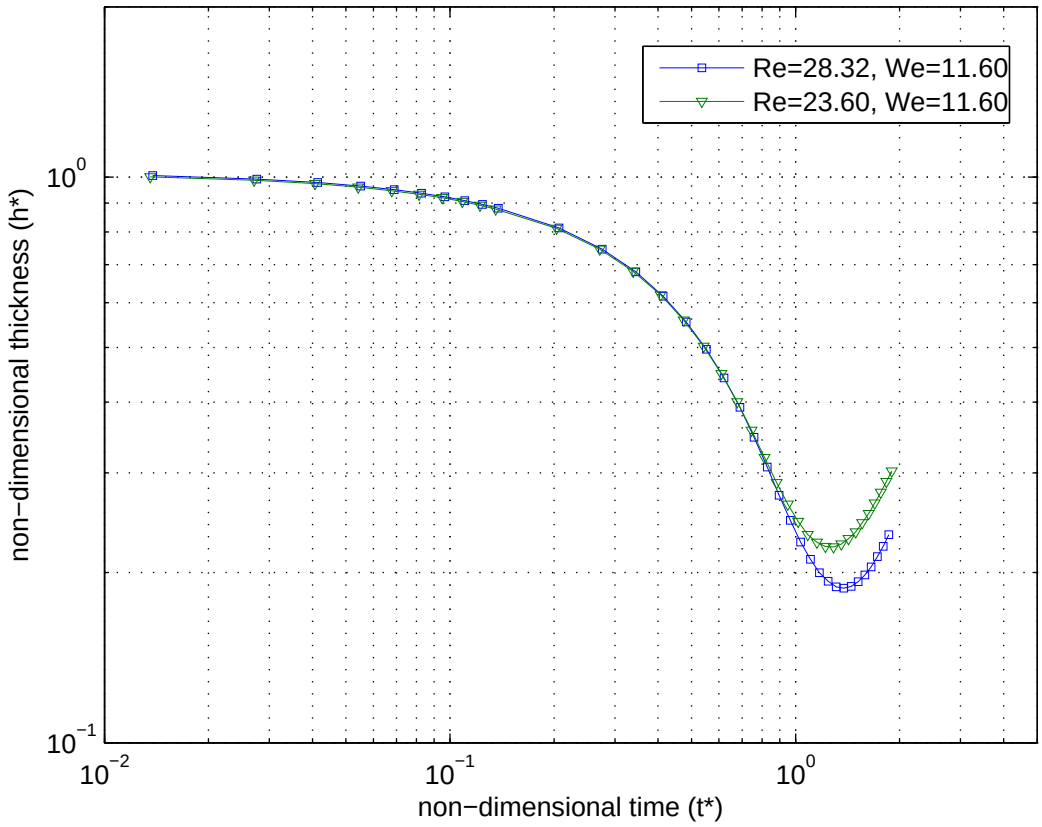

Re=28.32, We=11.60
Re=23.60, We=11.60
non−dimensional thickness (h*)
non−dimensional time (t*)
10^0
10^−1
10^−2
10^−1
10^0

Figure 14

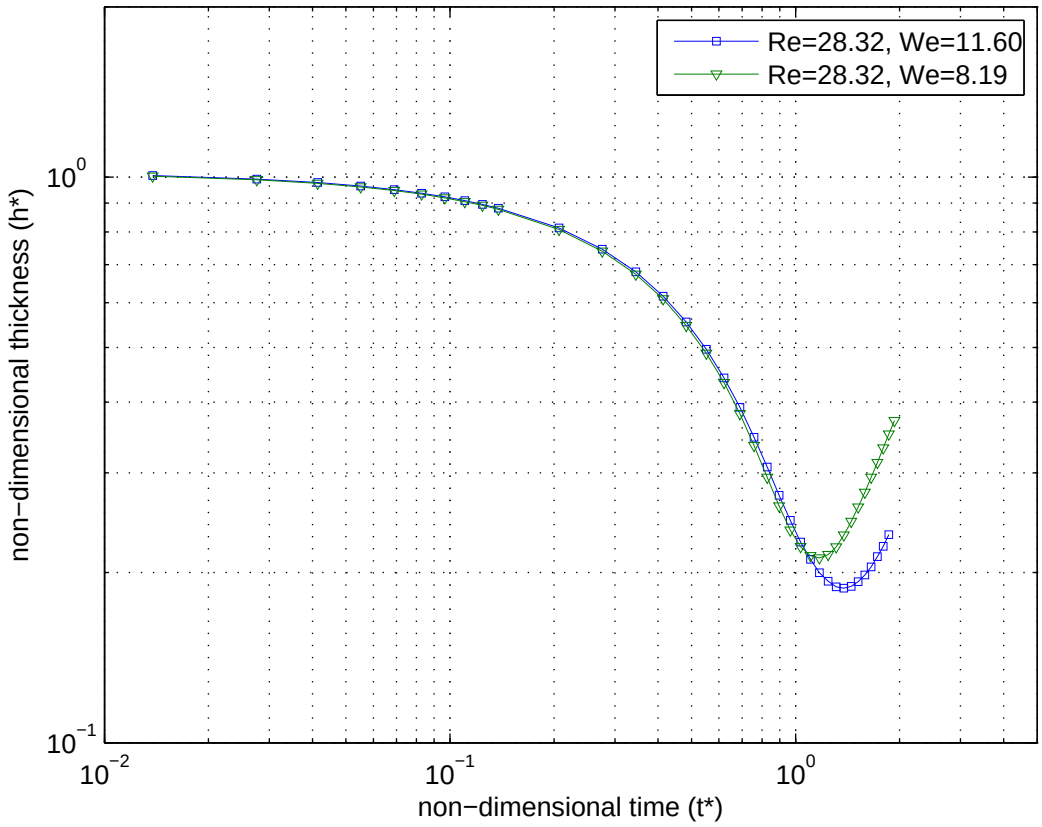

Re=28.32, We=11.60
Re=28.32, We=8.19
non−dimensional thickness (h*)
non−dimensional time (t*)
10^0
10^−1
10^−2
10^−1
10^0

Figure 15

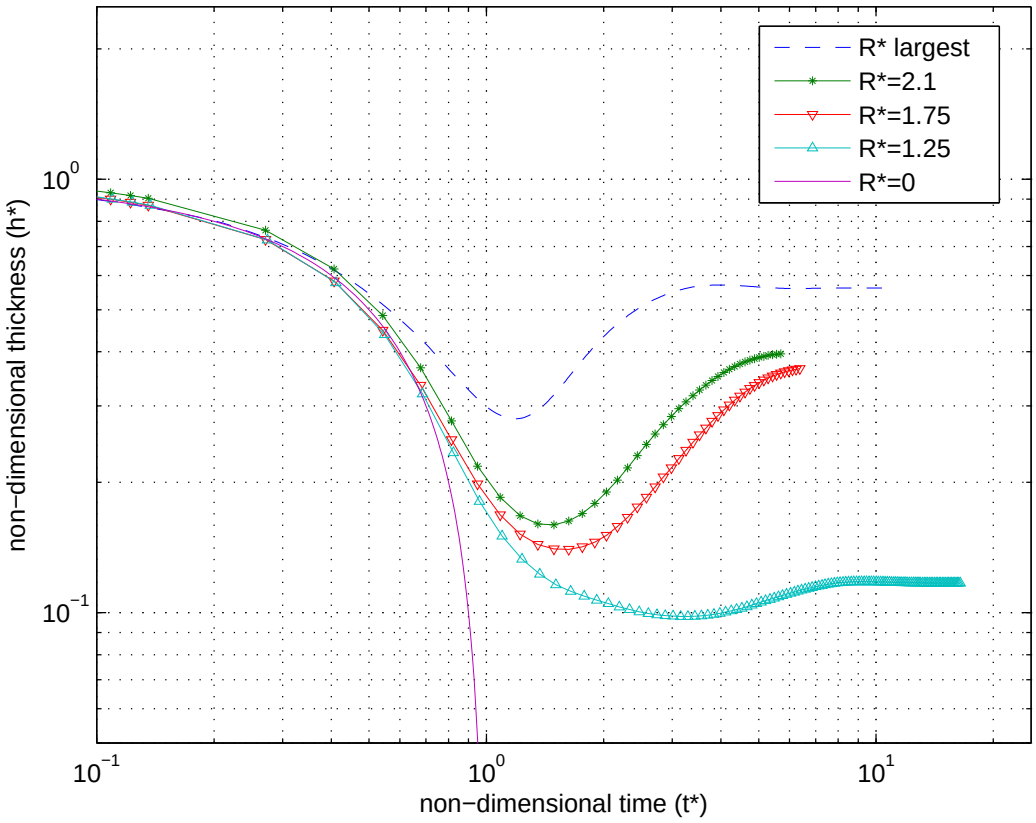

R* largest
R*=2.1
R*=1.75
R*=1.25
R*=0
non−dimensional thickness (h*)
non−dimensional time (t*)
10^0
10^−1
10^−1
10^0
10^1

Figure 16

Table 1: Simulation parameters.

Reynolds number	Weber number	Density ratio	Contact angle	a	b
27.72	10.86	240	90°	2/49	2/21
31.2	30.72	240	96°	0.5/49	3.5/21
41	52	240	96°	0.5/49	3.5/21
18.72	11.06	240	96°	0.5/49	3.5/21
54	104	114	104°	0.5/49	3.5/21
31.2	16	310	97°	1/49	2/21

Table 2: Summary of the simulation parameters for the cases of droplet impact onto a sphere.

Figure number	Re	We	Density ratio	Contact angle	Bond number	R*	a	b
10 - 12	42.48	26.14	328	76°	0.0908	1.23	1/49	2/21
	42.48	26.14	328	76°	0.0908	1.23	1/49	2/21
	42.48	26.14	328	76°	0.0908	1.23	1/49	2/21
13	42.48	26.14	328	76°	0.0908	1.23	1/49	2/21
	28.32	11.60	328	76°	0.0908	1.23	1/49	2/21
	23.36	7.90	328	76°	0.0908	1.23	1/49	2/21
14	28.32	11.60	328	76°	0	1.23	1/49	2/21
	23.60	11.60	328	76°	0	1.23	1/49	2/21
15	28.32	11.60	328	76°	0	1.23	1/49	2/21
	28.32	8.19	328	76°	0	1.23	2/49	2/21
16	28.32	11.60	328	76°	0.0908	1.25	1/49	2/21
	28.32	11.60	328	76°	0.0908	1.75	1/49	2/21
	28.32	11.60	328	76°	0.0908	2.1	1/49	2/21

Figure 1: Computational domain for the droplet impact on a flat surface.

Figure 2: Computational snapshots of the droplet impact on a flat surface; $We = 52$, $Re = 41$, density ratio=240, contact angle=96°.

Figure 3: Time evolution of the spread factor from the current lattice Boltzmann model simulation.

Figure 4: Time evolution of the spread factor in the kinematic phase for six different cases.

Figure 5: Comparison of the maximum spread factor predicted by the lattice Boltzmann model and various equations published in the literature.

Figure 6: Time evolution of the spread factor for $Oh = 0.177$.

Figure 7: Time evolution of the spread factor for $Re = 31.2$ and $\theta_w = 96°$.

Figure 8: Influence of wettability on the spreading behavior. ($Re = 31.2$, $We = 16$, density ratio is 313.

Figure 9: Computational domain for the droplet impact on a sphere.

Figure 10: Computational cross-section snapshots of the droplet impact on a sphere; $We = 26.14$, $Re = 42.48$, density ratio=328, contact angle=76°, $Bo = 0.0908$.

Figure 11: Computational 3D snapshots of droplet impact on a sphere; $We = 26.14$, $Re = 42.48$, density ratio=328, contact angle=76°, $Bo = 0.0908$.

Figure 12: Temporal variation of the film thickness at the north pole of the sphere; $We = 26.14$, $Re = 42.48$, density ratio=328, contact angle=76°, $Bo = 0.0908$.

Figure 13: Temporal variation of the film thickness at the north pole of the sphere for different Reynolds and Weber numbers. The value of $R^\star = 1.23$, $Bo = 0.0908$ and wettability is 76°.

Figure 14: Temporal variation of the film thickness at the north pole of the sphere for different Reynolds number.

Figure 15: Temporal variation of the film thickness at the north pole of the sphere for different Weber numbers.

Figure 16: Temporal variation of the film thickness at the north pole of the sphere for

different target-to-drop size $R^{\star}$. The value of $Re = 28.32$, $Bo = 0.0908$ and wettability is 76°.

Table 1: Simulation parameters.

Table 2: Summary of the simulation parameters for the cases of droplet impact onto sphere.



https://dspace.org/

Application of a high density ratio lattice-Boltzmann model for the droplet impingement on flat and spherical surfaces

Zhang, Duo; Papadikis, Konstantinos; Gu, Sai

2014-06-06
Elsevier
http://dx.doi.org/10.1016/j.ijthermalsci.2014.05.002
Duo Zhang, K. Papadikis, Sai Gu, Application of a high density ratio lattice-Boltzmann model for the droplet impingement on flat and spherical surfaces, International Journal of Thermal Sciences, Volume 84, October 2014, Pages 75-85

Downloaded from a DSpace repository. https://dspace.org/